

# A CFD Validation Challenge for Transonic, Shock-Induced Separated Flow: Experimental Characterization

Kyle P. Lynch<sup>1</sup>, Blake Lance<sup>2</sup>, Gyu Sub Lee<sup>3</sup>, Jonathan W. Naughton<sup>4</sup>, Nathan E. Miller<sup>5</sup>, Matt F. Barone<sup>6</sup>, Steven J. Beresh<sup>7</sup>, Russell W. Spillers<sup>8</sup>, and Melissa M. Soehnel<sup>9</sup>

*Sandia National Laboratories, Albuquerque, NM*

**An experimental characterization of the flow environment for the Sandia Axisymmetric Transonic Hump is presented. This is an axisymmetric model with a circular hump tested at a transonic Mach number, similar to the classic Bachalo-Johnson configuration. The flow is turbulent approaching the hump and becomes locally supersonic at the apex. This leads to a shock-wave/boundary-layer interaction, an unsteady separation bubble, and flow reattachment downstream. The characterization focuses on the quantities required to set proper boundary conditions for computational efforts described in the companion paper, including: 1) stagnation and test section pressure and temperature; 2) turbulence intensity; and 3) tunnel wall boundary layer profiles. Model characterization upstream of the hump includes: 1) surface shear stress; and 2) boundary layer profiles. Quantities on and downstream of the hump are intentionally withheld until completion of the validation challenge.**

## I. Introduction

There is continued emphasis on improving CFD predictions for separated, smooth-body, transonic flows. These flows contain unsteady shock and recirculation regions that challenge model-based approaches such as RANS, DES, LES, among others. The importance of capturing this set of physics has motivated a CFD validation challenge [1] for a transonic, separating flow test case. The challenge is structured such that the model and tunnel geometry, inflow conditions, and tunnel turbulence properties are provided to participants, but the experimental data near and in the wake of the hump is initially withheld. These data will be revealed only after all simulations have been completed. In this manner, various simulation approaches can be assessed while preventing a biased evaluation by removing the ability to calibrate a model to the experimental data *a priori*. Further, it allows for an evaluation of the variability between CFD estimates when the experimental data is unknown.

The test case is based on the classic axisymmetric transonic hump of Bachalo and Johnson [2], which consists of a spherical hump on a cylindrical body aligned with the wind tunnel operating at a high subsonic Mach number. A turbulent boundary layer develops along the cylindrical body, which accelerates as it approaches the hump. The flow becomes supersonic near the apex of the hump, forming a weak shock that imposes an adverse pressure gradient onto the incoming boundary layer. This causes it to separate, forming an unsteady separation bubble downstream of the hump which later undergoes an unsteady reattachment. This simple geometry is attractive for numerous reasons: first, axisymmetry removes questions related to sidewall interference for an equivalent 2D case; second, it remains a simple geometry for simulation purposes; and finally, the captured physics are directly applicable to numerous industry

<sup>1</sup> Senior Member of the Technical Staff, Aerosciences Department. Corresponding author: klynch@sandia.gov.

<sup>2</sup> Senior Member of the Technical Staff, V&V UQ and Credibility Processes Department.

<sup>3</sup> Graduate Student Intern, Aerosciences Department.

<sup>4</sup> Professor of Mechanical Engineering, University of Wyoming.

<sup>5</sup> Senior Member of the Technical Staff, Aerosciences Department.

<sup>6</sup> Principal Member of the Technical Staff, Aerosciences Department.

<sup>7</sup> Distinguished Member of the Technical Staff, Aerosciences Department.

<sup>8</sup> Principal Technologist, Aerosciences Department.

<sup>9</sup> Test Operations Engineer, Aerosciences Department.

Sandia National Laboratories is a multimission laboratory managed and operated by National Technology & Engineering Solutions of Sandia, LLC, a wholly owned subsidiary of Honeywell International Inc., for the U.S. Department of Energy's National Nuclear Security Administration under contract DE-NA0003525. This paper describes objective technical results and analysis. Any subjective views or opinions that might be expressed in the paper do not necessarily represent the views of the U.S. Department of Energy or the United States Government.

applications, for example, aircraft wings at cruise condition. Therefore, the case is a good candidate for transonic CFD validation.

The Bachalo and Johnson geometry was tested in the NASA Ames 2 ft. x 2 ft. and 6 ft. x 6 ft. transonic facilities and comprised multiple diagnostics: surface oil-flow visualization, Schlieren/interferometric imaging, surface pressure taps, and a traversing laser-Doppler anemometer (LDA). This allowed for measurement of the mean surface pressure coefficient, separation bubble size, mean velocity and turbulent stresses, and some derived properties such as turbulent mixing length. However, as noted by Spalart et al. [3], this experiment did not produce data on skin-friction, and only limited data on flow unsteadiness, shock location, and higher-order turbulent statistics. An additional omission in the experiment was a detailed characterization of the inflow conditions such as freestream turbulence intensity, which is critical in the context of computational validation studies.

This work revisits the Bachalo-Johnson experiment, with four primary goals: first, to extend data on surface pressure, velocity field, and turbulent statistics; second, to apply modern diagnostic techniques such as particle image velocimetry, fast pressure-sensitive paint, and oil film interferometry to quantify the velocity field, unsteady pressure, and surface shear stress; third, to rigorously document the tunnel conditions for use as suitable simulation boundary conditions; and fourth, to run the experiment at a lower Reynolds number that is more tractable for high-fidelity computations. Due to the reduced Reynolds number and different wind tunnel configuration (see following section), we caution that this experiment is *not* meant to be an exact replica of Bachalo-Johnson, but a standalone, separate experiment containing similar flow physics subjected to tunnel wall effects that should be included in any validation effort.

Section 2 describes the tunnel and model configuration. In section 3, the suite of diagnostics used for the characterization are detailed. Finally, section 4 provides selected data on the wind tunnel flow conditions and upstream model conditions. This selection of data allows for the proper boundary conditions to be applied in the context of the CFD challenge. Details on the challenge itself and quantities of interest in the comparison can be found in the companion paper.

## II. Model Design

The experiment is run in the Sandia Trisonic Wind Tunnel (TWT). The TWT is a blowdown-to-atmosphere facility using air as the test gas with interchangeable test sections. It can achieve subsonic Mach numbers from 0.5 to 1.3 using a variable downstream choke. The test section is a rectangular duct of dimensions 12 in  $\times$  12 in enclosed within a plenum to accommodate ventilated test section configurations. The TWT has a run time of 30–40 sec with 20–30 min between runs. For transonic operation, the stagnation pressure can be varied between approximately 16–35 psig, and reservoir heating maintains a stagnation temperature approximately 100–120 °F during a run. Either solid or porous walls may be used; for this experiment, solid walls are chosen to provide a simplified boundary condition for simulations. This poses geometrical restrictions related to tunnel blockage as discussed below. Detailed wind tunnel geometry will be provided at the start of the validation challenge.

The TWT is smaller than the NASA Ames 6 ft  $\times$  6 ft and 2 ft  $\times$  2 ft tunnels used by Bachalo and Johnson [2]. The reduced scale of the wind tunnel requires a scaled-down model. Uzun and Malik [4] describe geometric ambiguities in the model definition given by Bachalo and Johnson, particularly regarding the intersection of the hump with the model. Therefore, an analytical definition of the geometry is proposed; a schematic is given in figure 1. The geometry consists of a cylindrical body of diameter  $d$  capped by an elliptical nose of length  $a$ . At location  $a_t$ , a step of height  $t$  fixes the transition location. Following the nose is a constant-diameter forebody of length  $b$ . The hump is defined as a circular section of radius  $R_1$  and chord  $c$ . It intersects the forebody using a circular fillet of radius  $R_2$  tangent to both the forebody and hump. The hump intersects a constant-diameter afterbody with no fillet, and the afterbody continues length  $e$  to the sting mount of the wind tunnel.

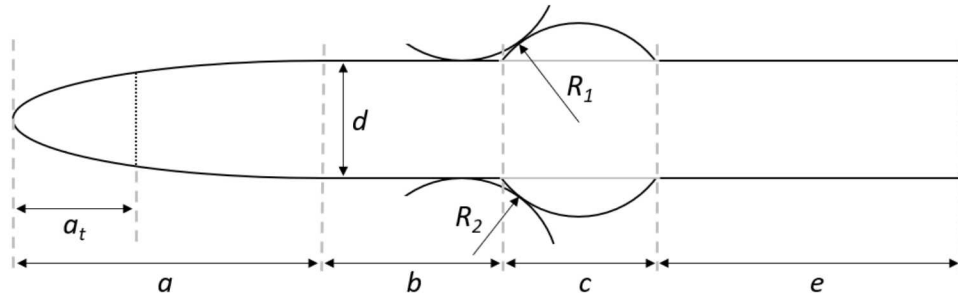


**Figure 1.** Schematic diagram of model. Flow is from left to right.

The exact values of the geometry as well as a detailed analytical description and code to generate the geometry are given in appendix A. The tunnel conditions and geometry quantities are defined to match features of the Bachalo-Johnson configuration such as an incoming Mach number of 0.875, while some additional geometrical constraints are imposed to prevent wind tunnel blockage at the high Mach number. Based on this geometry and the tunnel operational envelope, the target Reynolds number based on chord  $c$  is 1 million. It is machined from 7075-T6 aluminum. It is sting mounted over 8 chord lengths downstream of the hump, and far upstream of the tunnel choke location.

### III. Diagnostic Approach

#### A. Pressure and Temperature

The steady distribution was measured using a 64-port electronic pressure scanner (Kulite KMPS-1-64). The unit consists of 32 ports with a 5 psid range, 16 ports with 25 psid range, and 16 ports with 15 psia range. The total error of each port is  $\pm 0.1\%$  of the full-scale value. Values were read directly using a digital readout over Ethernet. The 32 static pressure taps along the test section wall were connected to the 5 psid range. Two taps in the top and bottom of the stagnation chamber were connected to the 25 psid range. Also connected to the 25 psid range were the model-mounted pressure taps upstream of the hump. The reference pressure for all gage sensors was plumbed to atmosphere and was simultaneously measured using one port of 15 psia range.

Stagnation temperatures were measured using two type-T thermocouples measured using a NI-9212 cDAQ module. Two Medtherm type-T coaxial thermocouples were fixed to the surface of the model to evaluate the model temperature during a run. These were measured using a separate NI-9212 module.

#### B. Oil-Film Interferometry

Surface shear stress is measured via oil-film interferometry. This technique has been successful in numerous configurations, including high-speed compressible flows [5]. It has also been used to provide skin friction data on the NASA 2D hump configuration by Naughton et al. [6]. Illumination is provided using a mercury-vapor grid lamp (BHK 88-9102-02), passing through frosted diffuser glass. A 50/50 beamsplitter is used to orient the illumination together with the imaging. An Imperx IPX-2M30H-G monochrome camera (1920 x 1080 px, 7.4  $\mu\text{m}$  pixel size), is used for imaging with a 35 mm C-mount lens. A Thorlabs FL543.5-10 bandpass filter (center wavelength 543.5 nm  $\pm 2$  nm, full-width half-max 10  $\pm 2$  nm) is attached to the lens to select the 546.1 nm atomic emission line of the mercury lamp. Dow Xiameter PMX-200 silicone oil was used, with a nominal 200 cSt viscosity. The temperature dependence of the viscosity and density was independently calibrated using an Anton Paar stabinger viscometer.

Photogrammetry was applied to properly scale the image data prior to processing [7]. Analysis was then conducted using the multi-image method of Naughton and Hind [8]. Oil was applied at multiple locations on the model, allowing for a continuous description of the skin friction on the forebody.

#### C. Particle Image Velocimetry

Planar particle image velocimetry is used to characterize the tunnel turbulence level and incoming boundary layers on the tunnel wall and on the model. The PIV arrangement consists of a LaVision Imager sCMOS camera (2560 x 2160 px at 50 Hz, 6.5  $\mu\text{m}$  pixel size) and a Quantel Evergreen HP laser (2 x 310 mJ/pulse at 25 Hz). Seeding is provided by a Corona Vi-count 5000 thermal smoke generator, producing large quantities of particles of approximately 0.7-0.8  $\mu\text{m}$  diameter as measured in other test campaigns using a shock-wave test.

The small size of the boundary layer upstream of the hump requires a high-magnification setup to adequately resolve. For the incoming boundary layer and turbulence intensity, a Nikon 200mm f/4 Micro-NIKKOR lens and a 2:1 teleconverter provide a magnification of approximately 1.5 (267 px/mm) at a camera working distance of approximately 12 in. To accommodate this short working distance, the optical setup is ‘folded’ into the tunnel plenum, using a large laser line mirror to redirect the image to the camera. The same folded arrangement is used for the tunnel wall boundary layer measurements, but with a 105 mm lens to yield a magnification of 0.4 (64 px/mm).

### IV. Experimental Characterization

Measurements are presented to characterize boundary conditions needed in CFD simulations and to help set tunable parameters such as turbulence transition locations. The authors caution that the data presented here supersedes data previously reported in an earlier paper [1]. The location of the model in the tunnel has changed since that earlier work. Therefore, participants should use the current results to tune their solutions.

#### A. Tunnel Conditions: Stagnation Pressure

The TWT is a blowdown facility, requiring multiple runs in order to build statistical datasets and for various measurements. Small variations in control valve performance between runs lead to variations in the stagnation pressure between and during each run. The stagnation pressure time-history for all runs is shown in figure 2. Note, runs have varying durations due to the time requirements for specific measurements. To distill the varying stagnation pressure to a bounded interval for use in CFD simulations, the statistics of all pressure samples were compiled as shown in figure 2, right. Each run is described by a histogram of measurement samples, and all runs are compiled into a cumulative histogram. The distribution is specified by a mean stagnation pressure value computed as a mean of all samples, and 2.5% and 97.5% percentile bounds. These are combined with the measurement bias uncertainty as described in appendix B to set the final interval. The bias uncertainty of the transducer is 0.1724 kPa, yielding a reported value of stagnation pressure: [REDACTED]

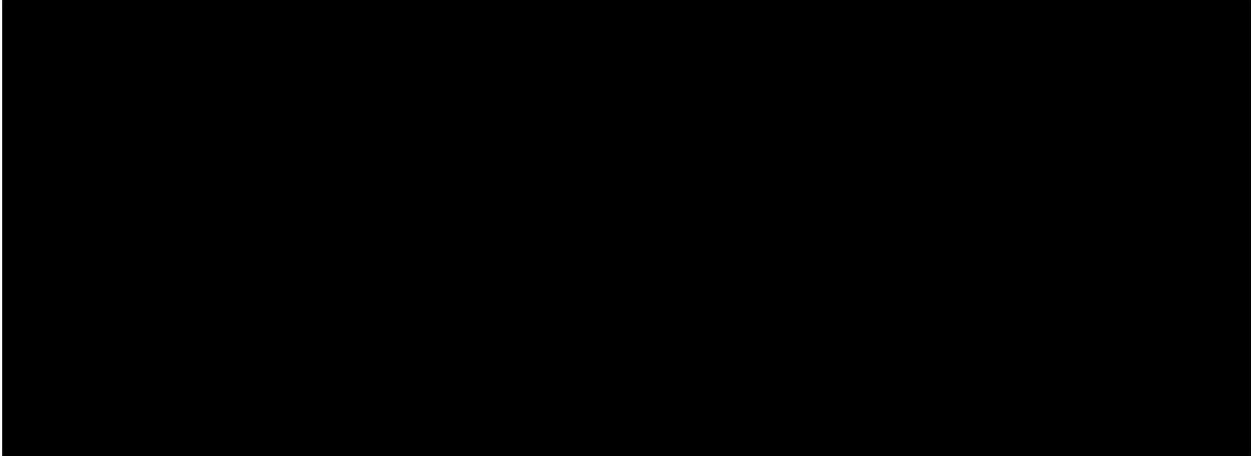


**Figure 2.** Left, time-history of stagnation pressure for all runs. Error bars correspond to the bias uncertainty of 0.1724 kPa for the pressure transducer. Error bars only plotted on one run for clarity but are representative of all runs. Right, histograms for all runs, including the cumulative histogram. Mean value and 2.5-97.5% percentiles shown.

#### B. Tunnel Conditions: Stagnation Temperature

The stagnation temperature exhibits variation between and during runs. This is primarily due to the thermal mass of unheated pressure lines between the facility and the heated air reservoirs. It takes roughly 25 seconds for temperature to reach a steady state, which then begins to decrease due to constant-volume expansion from the reservoirs. The stagnation temperature is shown to the left of figure 3. Variations of around 10 K occur within a run. The same histogram approach is taken to quantify the sample distribution in the right of figure 3. These percentiles are combined with the bias uncertainty of the thermocouple and DAQ (2.15 K) to yield the reported value of stagnation temperature: [REDACTED]



**Figure 3.** Left, time-history of stagnation temperature for all runs. Error bars correspond to bias uncertainty of 2.15 K in the temperature measurement. Error bars only plotted on one run for clarity but are representative of all runs. Right, histograms of temperature samples for all runs (in color). Cumulative histogram given as outline. Mean and 2.5-97.5% percentiles shown.

### C. Tunnel Conditions: Wall Pressure Ratio and Mach Number

The use of a solid-wall test section results in a significant non-uniform pressure distribution along the wall compared to a porous-wall test section. Due to model blockage and boundary layer growth on the tunnel wall and model, the Mach number increases between 5-10% at the streamwise stations corresponding to the model (see i.e., figure 6 in [1]). As the upstream Mach number increases, a nearly-choked condition is created, limiting the upstream Mach number for this model size. The nonuniformity makes the definition of a ‘freestream’ or ‘far-field’ flow condition ambiguous. Therefore, we provide a specific, measurable definition: ***the reference pressure ratio and Mach number are defined as the condition at the tunnel wall at a streamwise station corresponding to  $x/c = 0$*** . These conditions will be denoted by the subscript  $w,x/c = 0$ . CFD challenge entrants are requested to tune the parameters of their model to match this reference pressure ratio.

A similar statistical procedure is applied to define the reference pressure ratio. Note, the pressure ratio is being reported, not the absolute value of pressure. Between and during runs, variations in wall static pressure track variations in stagnation pressure. Therefore, the pressure ratio exhibits reduced statistical variation and is better suited as a reference quantity. On the left of figure 4, an overlay is presented of the  $x/c = 0$  wall port pressure ratio for all runs, and the statistical analysis is on the right of figure 4.

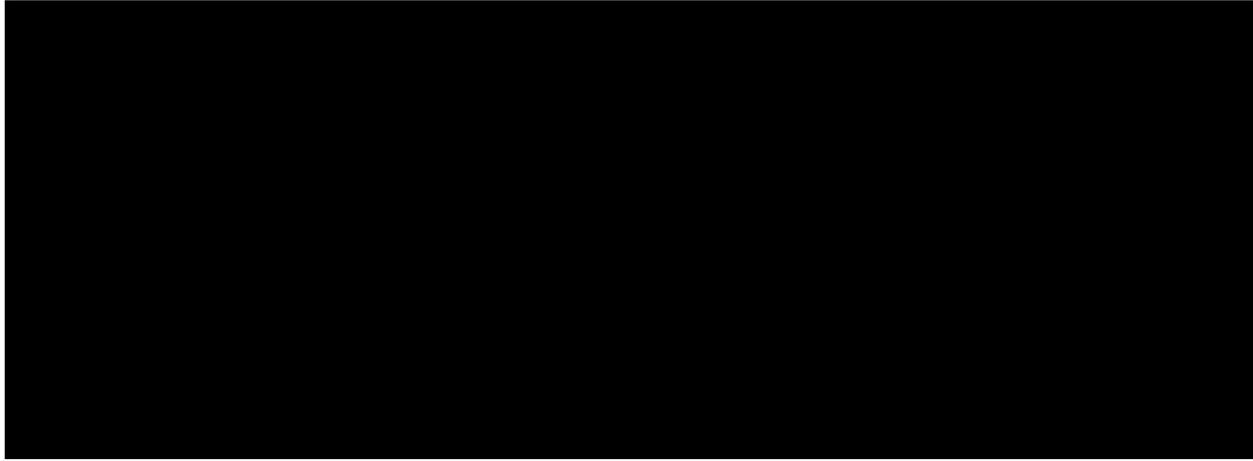


**Figure 4.** Left, time-history of wall pressure ratio at  $x/c = 0$  for all runs. Right, histograms of pressure ratio samples for all runs (in color). Cumulative histogram given as outline. Mean and 2.5-97.5% percentiles shown.

The Mach number is reported as a derived quantity in figure 5. It is calculated using isentropic relations based on the  $x/c = 0$  wall port pressure ratio and a constant ratio of specific heats,  $\gamma = 1.4$ . The stability and repeatability of the Mach number is within approximately 0.002. This is on the order the uncertainty of the measurement of 0.0017. The

bias uncertainty propagation of pressure ratio to Mach number is given in Appendix B. Note, participants are encouraged to use the pressure ratio for tuning their models, rather than the derived Mach number; the latter is given here for informational purposes.

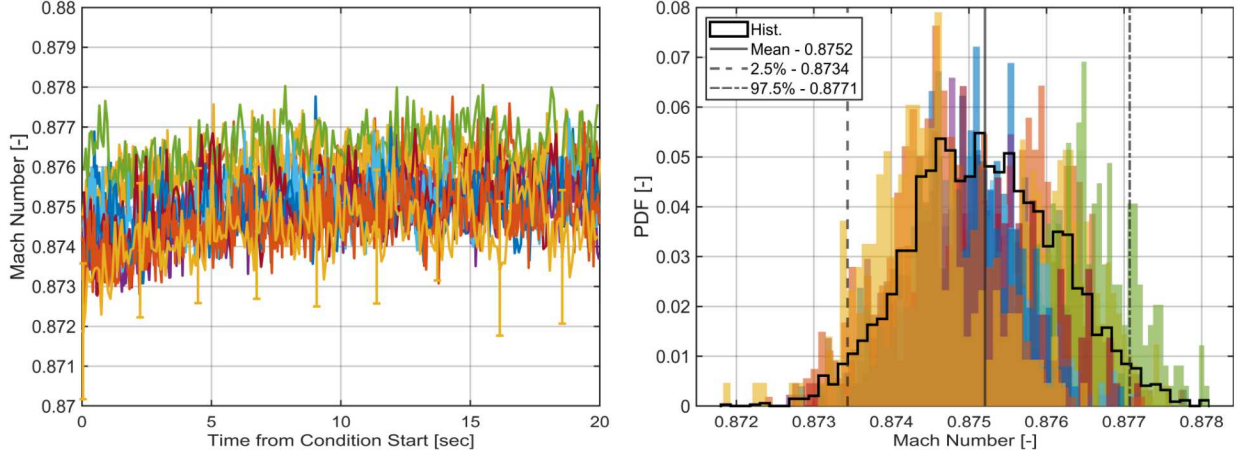


**Figure 5.** Left, time-history of Mach number at the tunnel wall at  $x/c = 0$  for all runs. Error bars correspond to the uncertainty in the pressure measurement propagated through to Mach number. Error bars only plotted on one run for clarity but are representative of all runs. Right, histograms of Mach number samples for all runs (in color). Cumulative histogram given as outline. Mean and 2.5-97.5% percentiles shown.

#### D. Tunnel Conditions: Reynolds Number

The Reynolds number is provided as a derived quantity to assist participants in setting parameters of their models. The isentropic relations yield temperature and density at  $x/c = 0$  based on the tunnel wall pressure ratio at  $x/c = 0$ . Sutherland's law is used for dynamic viscosity. Results are shown in figure 6.

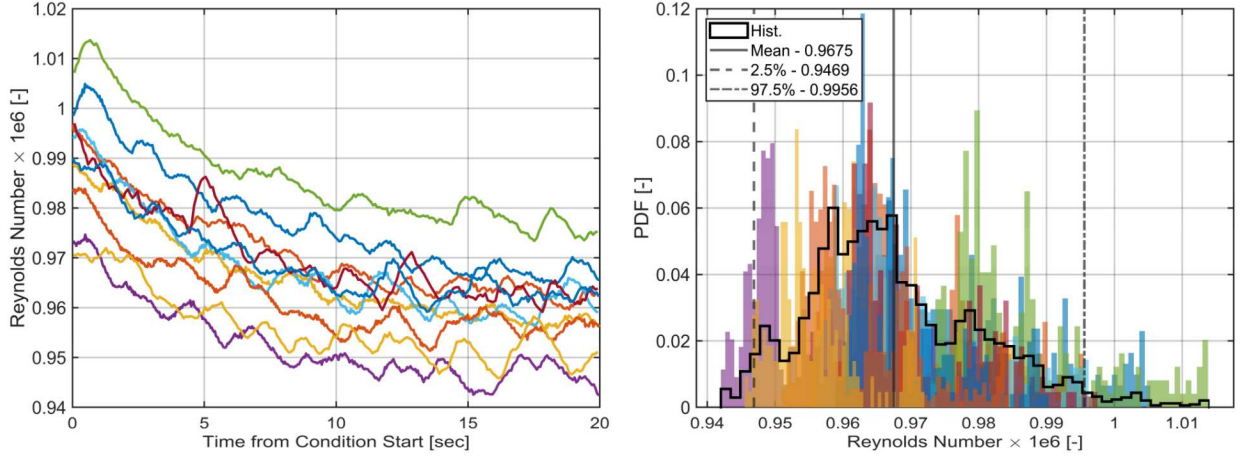


**Figure 6.** Left, time-history of Reynolds number at the tunnel wall at  $x/c = 0$  for all runs. Right, histograms of Reynolds number samples for all runs (in color). Cumulative histogram given as outline. Mean and 2.5-97.5% percentiles shown.

#### E. Tunnel Turbulence Intensity

The turbulence intensity measurement was conducted following the method proposed by Scharnowski et al. [9], where multiple measurements at different  $\Delta t$  are used to unambiguously determine turbulence intensity in the presence of measurement noise. Six runs of 500 image pairs each were used to build the required statistics, with processing conducted using an iterative image deformation method with a range of window sizes from 24 px (0.09 mm) to 256 px (0.95 mm) and a suitable initial predictor to capture the large displacements for longer  $\Delta t$ ; results are shown in figure 7. The method yields similar turbulence intensity of 0.228% across a range of window sizes and correctly captures the increase in random noise as the window size is reduced. The uncertainty is conservatively estimated at  $\pm 0.01\%$ , based on the variability of the measurement with window size.

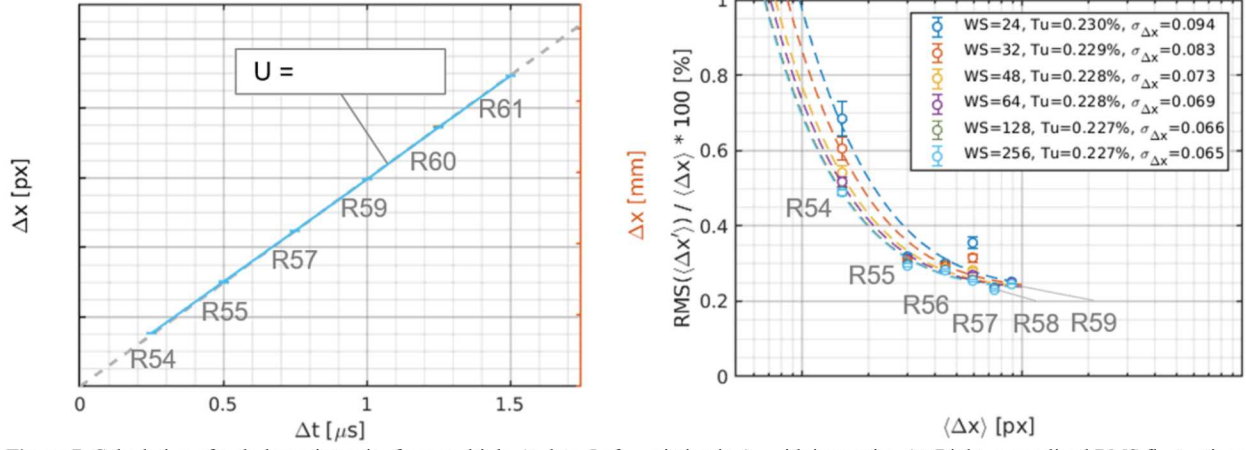


**Figure 7.** Calculation of turbulence intensity from multiple- $\Delta t$  data. Left, variation in  $\Delta x$  with increasing  $\Delta t$ . Right, normalized RMS fluctuations of  $\Delta x$ . Dashed lines are from model of Schamowski et al. [11].

#### F. Tunnel Conditions: Summary

The reported conditions in the previous sections are summarized in table 1. As detailed in the companion paper, participants are encouraged to submit results utilizing the mean value and the edges of the uncertainty bounds, in order to assess the variability of simulations. Propagating boundary condition uncertainty through CFD models enables more conclusive validation comparisons. For example, differences in results within the experimental uncertainty suggest that model form error is within the uncertainty and likely acceptable if the uncertainties are sufficiently small for the intended use of the model. On the other hand, if the differences are outside the uncertainties, then model form error is relatively large and model improvement efforts would prove worthwhile. Note that systematic/bias sources and the random uncertainties sources were combined by RSS (root-sum-square) as in Coleman and Steele [10].

**Table 1:** Tunnel boundary conditions. Rows in grey correspond to derived quantities that should be used for reference only.

	Mean	Uncertainty
<b>Stagnation Pressure, <math>p_0</math></b>		
<b>Stagnation Temperature, <math>T_0</math></b>		
<b>Wall Pressure Ratio, <math>p_{w,x/c=0}/p_0</math></b>		
<b>Wall Mach Number, <math>M_{w,x/c=0}</math></b>		
<b>Wall Reynolds Number, <math>Re_{w,x/c=0}</math></b>		
<b>Tunnel Wall Boundary Layer Thickness, <math>\delta_{99,x/c=0}</math></b>		
<b>Turbulence Intensity</b>		

#### G. Upstream Model Surface Shear Stress

The forebody surface skin-friction results as measured using OFI are given in figure 8. Measurements range from of  $x/c = -1$  to  $x/c = -0.5$ , compiled from multiple measurements with different locations for oil application. As expected for a growing boundary layer, the skin friction decreases along the streamwise direction.

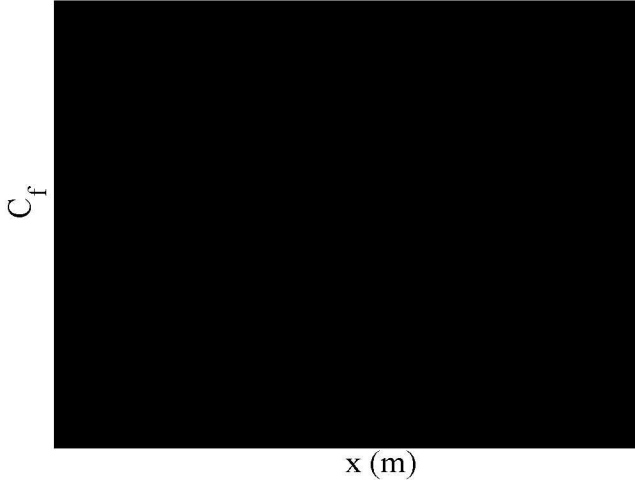


**Figure 8.** Skin-friction coefficient along the forebody of the model. Data is from multiple runs with oil applied at different streamwise locations.

## Conclusions

A database of measurements suitable for use as boundary conditions and calibration data are provided in the context of the CFD challenge on the Sandia Axisymmetric Transonic Hump. Measurements included stagnation temperature and pressure, wall pressure, upstream model pressure, upstream surface shear stress distributions, upstream model and tunnel boundary layer distributions, and model temperature. Participants are advised to read the companion paper for information on the structure of the challenge and submission requirements.

## Acknowledgements

The authors thank the Sandia CFD challenge advisory committee, consisting of Chris Roy, Lian Duan, Jonathan Naughton, and Barton Smith, for their helpful comments prior to the measurement campaign.

## References

- [1] K. Lynch, N. Miller, M. Barone, S. Beresh, R. Spillers, J. Henfling and M. Soehnel, "Revisiting Bachalo-Johnson: The Sandia Axisymmetric Transonic Hump and CFD Challenge," *AIAA Paper 2019-2848*, 2019.
- [2] W. D. Bachalo and D. A. Johnson, "Transonic, Turbulent Boundary-Layer Separation Generated on an Axisymmetric Flow Model," *AIAA J*, pp. 437-443, 1986.
- [3] P. Spalart, K. Belyaev, A. Garbaruk, M. Shur, M. Strelets and A. Travin, "Large-eddy and Direct Numerical Simulations of the Bachalo-Johnson flow with Shock-Induced Separation," *Flow Turb Combust*, vol. 99, pp. 865-885, 2017.
- [4] A. Uzun and M. Malik, "Wall-Resolved Large-Eddy Simulations of Transonic Shock-Induced Flow Separation," *AIAA J*, vol. 57, no. 5, 2019.
- [5] J. W. Naughton and M. Sheplak, "Modern developments in shear-stress measurement," *Progress in Aerospace Sciences*, vol. 38, pp. 515-570, 2002.
- [6] J. W. Naughton, S. Viken and D. Greenblatt, "Skin-Friction Measurements on the NASA Hump Model," *AIAA J*, vol. 44, no. 6, pp. 1255-1265, 2006.
- [7] J. W. Naughton and T. Liu, "Photogrammetry in Oil-Film Interferometry," *AIAA Journal*, vol. 45, no. 7, 2007.

- [8] J. W. Naughton and M. D. Hind, "Multi-image oil-film interferometry skin friction measurements," *Measurement Science and Technology*, vol. 24, no. 12, 2013.
- [9] S. Scharnowski, M. Bross and C. J. Kahler, "Accurate turbulence level estimations using PIV/PTV," *Experiments in Fluids*, vol. 60, no. 1, 2019.
- [10] H. W. Coleman and W. G. Steele, *Experimentation, Validation, and Uncertainty Analysis for Engineers*, Hoboken: Wiley, 2009.

## Appendix A: Geometry Definition

### A.1. Geometry Quantities

The geometry is defined using the values in table 2.

**Table 2:** Geometry information for the model.

Parameter	Value
Step Position ( $a_t$ )	10.0
Step Height ( $t$ )	1.0
Nose Length ( $a$ )	10.0
Cylinder Diameter ( $d$ )	1.0
Radius Before Step ( $r_{before}$ )	0.5
Radius After Step ( $r_{after}$ )	0.5
Radius of Hump (Red) ( $r_h$ )	0.5
Radius of Hump (Blue) ( $r_h'$ )	0.5
Radius of Downstream Cylinder ( $r_d$ )	0.5
Radius of Upstream Fillet ( $r_f$ )	0.5
Length of Hump ( $L_h$ )	10.0
Length of Downstream Cylinder ( $L_d$ )	10.0
Length of Upstream Fillet ( $L_f$ )	1.0
Width of Hump ( $w_h$ )	1.0
Width of Downstream Cylinder ( $w_d$ )	1.0
Width of Upstream Fillet ( $w_f$ )	1.0
Height of Hump ( $h_h$ )	1.0
Height of Downstream Cylinder ( $h_d$ )	1.0
Height of Upstream Fillet ( $h_f$ )	1.0
Radius of Hump (Blue) ( $r_h'$ )	0.5
Radius of Downstream Cylinder ( $r_d$ )	0.5
Radius of Upstream Fillet ( $r_f$ )	0.5
Length of Hump ( $L_h$ )	10.0
Length of Downstream Cylinder ( $L_d$ )	10.0
Length of Upstream Fillet ( $L_f$ )	1.0
Width of Hump ( $w_h$ )	1.0
Width of Downstream Cylinder ( $w_d$ )	1.0
Width of Upstream Fillet ( $w_f$ )	1.0
Height of Hump ( $h_h$ )	1.0
Height of Downstream Cylinder ( $h_d$ )	1.0
Height of Upstream Fillet ( $h_f$ )	1.0

### A.2. Elliptical Nose with Step Definition

The elliptical nose is defined by the nose length  $a$ , cylinder diameter  $d$ , the step height  $t$ , and step position  $a_t$ . The model radius before and after the step is given by,

$$\begin{aligned} x \leq a_t: y &= \left(\frac{d}{2} + t\right) \sqrt{1 - \frac{x^2}{a^2}} \\ x > a_t: y &= \frac{d}{2} \sqrt{1 - \frac{x^2}{a^2}} \end{aligned} \quad (1)$$

### A.3. Hump Definition

The hump definition consists of two circular contours as shown in figure 9. The first (red) describes an upstream transition fillet and the second (blue) provides the remainder of the hump shape to the downstream cylinder intersection. These are connected at their tangent point  $(x_t, y_t)$ .

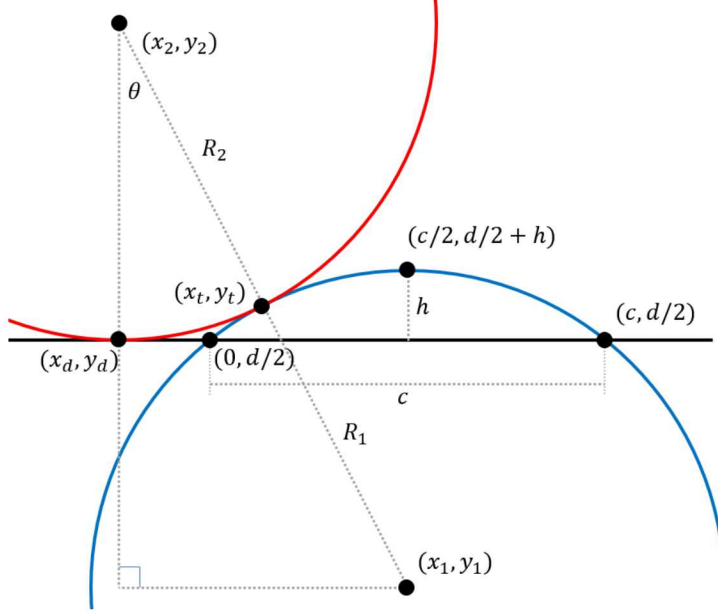


**Figure 9.** Geometry definitions for the hump.

The center coordinates of the main hump at  $(x_1, y_1)$  are calculated from three points on the surface of the cylinder:  $(0, d/2)$ ,  $(c/2, d/2 + h)$ , and  $(c, d/2)$ , where  $c$  is the hump chord and  $h$  is the hump height. These constants to be released during the final geometry specification. These points yield of the intersection of the normals of two chord lines via,

$$m_a = \frac{2h}{c}$$

$$m_b = \frac{-2h}{c}$$

$$(x_1, y_1) = \left( \frac{\frac{m_b c}{2} - \frac{3m_a c}{2}}{2(m_b - m_a)}, -\frac{1}{m_a} \left( x_1 - \frac{c}{4} \right) + \frac{d+h}{2} \right) \quad (2)$$

$$R_1 = \sqrt{x_1^2 + \left( \frac{d}{2} - y_1 \right)^2}$$

The fillet circle radius is defined as  $R_2 = c_f d$ , where  $c_f$  is a constant to be released during final geometry specification. This yields for the center position of the fillet circle,

$$(x_2, y_2) = \left( x_1 - \sqrt{(R_1 + R_2)^2 - \left( R_2 + \frac{d}{2} - y_1 \right)^2}, y_1 \frac{d}{2} + R_2 \right) \quad (3)$$

Finally, the fillet start and transition locations are given by,

$$\theta = \text{atan} \frac{x_1 - x_2}{R_2 + \frac{d}{2} - y_1} \quad (4)$$

$$(x_t, y_t) = (x_1 - R_1 \sin \theta, y_1 + R_1 \cos \theta)$$

$$(x_d, y_d) = (x_2, \frac{d}{2})$$

#### A.4. Geometry Code

To aid implementations, a Matlab/Octave function which generates the profile as a function of streamwise position  $x$  is provided below,

```
function [r] = geom(x, a, b, c, d, e, h, t, at, rc)

% Define main hump based on chord and hump height.
ma = 2*h / c;
mb = -2*h / c;
x1 = (mb*c/2 - ma*3*c/2) / (2*(mb-ma));
y1 = -1/ma*(x1-c/4)+(d+h)/2;
R1 = sqrt(x1.^2 + (d/2-y1).^2);

% Calculate the tangent fillet.
R2 = rc*d;
x2 = x1 - sqrt( (R1 + R2)^2 - (R2 + d/2 - y1)^2 );
y2 = d/2 + R2;
theta = atan2(x1-x2, R2 + d/2 - y1);
xt = x1 - R1 * sin(theta);
xd = x2;

% Initialize coordinates.
r = zeros(1,length(x));

% Ellipse prior to step.
tmp = (x > -b-a+xd) & (x <= -b-a+xd+at);
r(tmp) = (d/2 + t)*sqrt(1-(x(tmp) + b - xd).^2./a.^2);

% Ellipse after step.
tmp = (x > -b-a+xd+at) & (x <= -b+xd);
r(tmp) = d/2*sqrt(1-(x(tmp) + b - xd).^2./a.^2);

% Forebody
tmp = (x > -b+xd) & (x <= xd);
r(tmp) = d/2;

% Fillet
tmp = (x > xd) & (x <= xt);
r(tmp) = y2 - sqrt(R2.^2 - (x(tmp)-x2).^2);

% Hump
tmp = (x > xt) & (x <= c);
r(tmp) = y1 + sqrt(R1.^2 - (x(tmp)-x1).^2);

% Afterbody
tmp = (x > c) & (x <= c+e);
r(tmp) = d/2;

end
```

## Appendix B: Uncertainty Propagation

The Mach number is a derived quantity from the isentropic relation,

$$M = \sqrt{\left[ \left( \frac{p_0}{p} \right)^{\frac{\gamma-1}{\gamma}} - 1 \right] \left( \frac{2}{\gamma-1} \right)}$$

where  $p_0$  is stagnation pressure,  $p$  is any arbitrary static pressure, and  $\gamma$  is the ratio of specific heats. The bias uncertainty propagation is performed with the Taylor Series Method (TSM) by Coleman and Steele [10] and considers the uncertainty of  $p_0$ ,  $p$ , and  $\gamma$ . Later  $\gamma$  is assumed as 1.4 for air. The general form of the TSM method applied to Mach number is therefore

$$U_M = \sqrt{\left(\frac{\partial M}{\partial \gamma}\right)^2 U_\gamma^2 + \left(\frac{\partial M}{\partial p_0}\right)^2 U_{p_0}^2 + \left(\frac{\partial M}{\partial p}\right)^2 U_p^2}$$

where  $U_i$  is the expanded uncertainty of parameter  $i$  and correlated uncertainties are not present. Here expanded uncertainty means that a confidence factor coefficient has been applied to the standard uncertainty and the commonly used factor in engineering is assumed to be 95% throughout this work,  $U_i = t_{95\%} u_i$ . The partial derivatives act as sensitivities between the parameter uncertainties and the uncertainty of the quantity of interest. Since  $U_\gamma \approx 0$ , we will skip solving the partial derivative  $\partial M / \partial \gamma$ . The remaining partial derivatives are solved as

$$\begin{aligned} \frac{\partial M}{\partial p_0} &= \frac{1}{\gamma p \left(\frac{p_0}{p}\right)^{\frac{1}{\gamma}} \sqrt{\left[\left(\frac{p_0}{p}\right)^{\frac{\gamma-1}{\gamma}} - 1\right] \left(\frac{2}{\gamma-1}\right)}} \\ \frac{\partial M}{\partial p} &= -\frac{p_0}{\gamma p^2 \left(\frac{p_0}{p}\right)^{\frac{1}{\gamma}} \sqrt{\left[\left(\frac{p_0}{p}\right)^{\frac{\gamma-1}{\gamma}} - 1\right] \left(\frac{2}{\gamma-1}\right)}} \end{aligned}$$

The simplified Mach number uncertainty general equation is therefore

$$U_M = \sqrt{\frac{p^2 U_{p_0}^2 + p_0^2 U_p^2}{\gamma^2 p^4 \left(\frac{p_0}{p}\right)^{\frac{2}{\gamma}} \left[\left(\frac{p_0}{p}\right)^{\frac{\gamma-1}{\gamma}} - 1\right] \left(\frac{2}{\gamma-1}\right)}}$$